Plasmonics
https://doi.org/10.1007/s11468-018-0767-6

# Near-Perfect Spectral Transmission Properties for Two Cascaded Plasmonic Ultrathin Nanograting Structures

Bo Zhao[1] · Jianjun Yang[2] · Zhenfen Huang[1]

Received: 2 March 2018 / Accepted: 14 May 2018


**Abstract**
A high-performance plasmonic transmission structure consisting of two longitudinally cascaded ultrathin metallic nanogratings with a half period lateral dislocated and separated by two heterogeneous dielectric layers is proposed and theoretically studied. Three near-unity spectral transmission peaks are observed for the cascaded plasmonic nanograting structure due to the evanescent field coupling of surface plasmon polariton waves supported by the two neighboring plasmonic nanogratings. The physical mechanism responsible for the near-perfect peak transmissions is discussed based on the corresponding spatial distributions of electromagnetic fields and is found to be two possible ways: by the excitation of hybrid anti-symmetric surface plasmon polariton leaky mode on the incident and transmission surfaces of the cascaded plasmonic nanograting structure or by the formation of localized surface plasmon polariton resonance modes within horizontally butt-jointed metal/insulator/metal coupled waveguides between the two cascaded plasmonic nanogratings. It is the two heterogeneous dielectric layers inserted between the two cascaded plasmonic nanogratings that is indispensable for the formation of the hybrid anti-symmetric surface plasmon polariton leaky mode, resulting in the near-unity transmission peak with an ultra-narrow bandwidth of 20 nm. The high-tunability of spectral transmission behaviors with varying structural parameters and dielectric layer are explored, which promise numerous potential applications in nano-optics devices, such as plasmonic filters, sensors, and nanoscale distance ruler.

**Keywords** Surface plasmon polariton · Metallic nanograting · Transmission · Leaky mode · Waveguide resonance mode

## Introduction

The spatially periodic distribution of the subwavelength structures on metallic films, which are assisted by the resonance behaviors of surface plasmon polariton (SPP), has been ever reported to show a physical phenomenon of extraordinary optical transmission (EOT) [1–3], and the resultant various exotic electromagnetic (EM) properties are promising for abundant of potential applications in optical devices, such as sensors [4], absorber [5], unidirectional coupler [6], and filters [7]. Physically, it has been identified that the resonance of SPP cavity mode and the coupled SPP mode make contributions to tunneling the light through the structures, resulting in EOT peaks in their transmission spectra [2]. If the thickness of metallic structured film is decreased to a semi-transparent scale, the excitation of SPP on the both input and output interfaces can be overlapped directly to create an anti-symmetric SPP bound mode, which consequently hinders the process of the light transmission, thus giving rise to the nearly-zero dips in the transmission spectra [8, 9].

Recently, multilayer metallic plasmonic structures, essentially composing of textured metallic films and dielectric layers, are utilized to perform some new exotic optical features due to the strong EM couplings between the two neighboring metallic layers via evanescent waves, which become absent in a single layer of metallic film. For instance, owing to the high sensitivity of the EM responses to the both lateral and longitudinal relative position, the dislocated double-cascaded metallic nanogratings separated by a dielectric/vacuum layer can be employed for the unidirectional couplers [10], nanoscale range findings [11], and refractive index sensors [12]. In addition, two cascading ultrathin metallic nanogratings with transversely butt-jointed metal/insulator/metal (MIM) cavities can be a candidate for the plasmonic spatial filter by the formation of localized SPP mode and SPP mode mixing system

✉ Jianjun Yang
jjyang@ciomp.ac.cn

[1] Department of Electronic Information and Physics, Changzhi University, Changzhi 046011, Shanxi, China

[2] Changchun Institute of Optics, Fine Mechanics and Physics, Chinese Academy of Sciences, Changchun 130033, China

Published online: 28 May 2018

[13]. Three-layer grating/insulator/metal (GIM) plasmonic structure, which is constituted by a ultrathin metallic grating and a seamless optical opaque metallic film with a spatial separation, can achieve a perfect selective absorption or thermal selective emission by exciting the localized SPP mode, which promises tremendous potentials for photonic devices, such as photodetectors, sensors, and photovoltaics [14–19]. If a seamless metallic film is designed to have ultrathin thickness to allow the light penetration, a transmission window begins to emerge owing to the induced strong magnetic resonance inside the GIM cavities [20], but its transmittance is usually far lower than the unity. Multiple-spectral transparent multilayer structure, which is composed of two plamonic nanogratings/nanoparticle arrays deposited on the two surfaces of a seamless ultrathin metal film or inserted between two seamless ultrathin metal films, has been theoretically investigated, and the observed near-unity multiple-spectral transmission phenomena were attributed to the hybridization effect of the SPP modes localized on the input and output plasmonic arrays [21–25]. Understanding of the SPPs coupling in the complex multiple-layer metallic structure is of fundamental interest and will have significant implications in design of the new functional nano-optic devices. However, the transmission of light through two cascaded asymmetric ultrathin metallic nanogratings based on the coupling of SPPs still remains less studied.

In this paper, we investigate the optical transmission properties of two dislocated ultrathin metallic nanogratings sandwiched with two heterogeneous dielectric layers, an air/vacuum layer and a high-permittivity dielectric one, in contrast to the systems during the previous studies. Our calculation results show that three near-unity transmission peaks are obtained due to the evident coupling of SPP waves confined on the two neighboring plasmonic nanogratings. The detailed analyses of the calculated EM field distributions give comprehensive insights into the physical mechanisms of the observed three near-perfect transmission peaks: one transmission peak with an ultra-narrow bandwidth is associated with hybrid antisymmetric SPP leaky mode; the other two transmission peaks with broader bandwidths are originated from localized SPP waveguide resonance modes. Finally, the optical responses of the spectral transmission for the cascaded plasmonic nanograting structures to the structural parameter variations and the permittivity of the sandwiched dielectric layer are explored as well.

## Simulation Method

A schematic diagram of a plasmonic multilayer structure that is composed of two sliver nanogratings cascading with an air separation (layer) $t_g$ and a dielectric layer of thickness $t_d$ associated with high permittivity $\varepsilon_2$ is illustrated in Fig. 1. Here, two heterogeneous dielectric layers are sandwiched between the two cascaded plasmonic nanogratings, resulting in asymmetric dielectric environment surrounding them. The whole multilayer structure is embedded into an air circumstance. The air separation can be replaced by a dielectric layer with the permittivity of $\varepsilon_1 = 1$ for the preparation of the cascaded structure. The two plasmonic nanogratings have the same periodicity of $\Lambda$; the slit (ridge) portion of the upper nanograting is laterally dislocated by a half period of $\Lambda/2$ with respect to that of the bottom one. The thicknesses of the two plasmonic nanogratings are $t_u$ and $t_b$, respectively. The slit widths in them are, respectively, $w_1$ and $w_2$. A series of horizontally butt-jointed MIM coupled waveguides are formed between the two cascaded nanogratings, wherein the input slit-aperture of width $w_1$ is laterally dislocated by a half period with respect to the output slit-aperture of width $w_2$. A TM-polarized plane wave with a Gaussian intensity profile, whose electric vector is perpendicular to the nanogratings, impinges the cascaded plasmonic nanograting structure from beneath at the normal incidence. The simulations are implemented by using a two-dimensional finite difference time domain (2D-FDTD) method. A relative permittivity of sliver with the dispersive properties is described by Drude model: $\varepsilon_{\mathrm{Drude}} = \varepsilon_\infty - \omega_p^2/\omega(\omega - i\gamma)$, wherein the constant of $\varepsilon_\infty = 3.7$, $\omega_p = 1.3673 \times 10^{16}$ rad/s, and $\gamma = 2.7325 \times 10^{16}$ rad/s are extracted from the tabulated data in the reference [26]. The upper and bottom boundaries of the simulation region are truncated by perfectly matched layers (PMLs), while the left and right sides are set with the periodic boundaries. The transmission spectrum is obtained by Fourier transformation of the time-domain EM fields, which is monitored by a linear detector placed behind the cascaded plasmonic nanograting structure. Normalized transmission is defined as the ratio of the time-averaged Poynting vector of the transmitted light to that of the incidence light. The wavelength range of the transmission spectrum is set as $\lambda = 400$–$2000$ nm. A monochromatic light is adopted for the incidence upon calculating EM field distribution maps around the structure.

## Results and Discussion

The calculated transmissions of the cascaded plasmonic nanograting structure as a function of the wavelength and slit width $w_2$ of the upper nanograting are shown in Fig. 2. The adopted geometric parameters and the dielectric permittivity are fixed as: $w_1 = 150$ nm, $t_b = t_u = 30$ nm, $t_d = 50$ nm, $t_g = 25$ nm, $\Lambda = 500$ nm, and $\varepsilon_2 = 3.9$. Note that the transmission spectrum of the isolated bottom nanograting with the high-permittivity dielectric layer (corresponding to the case of $w_2 = 500$ nm) is also given for comparison, as shown by the

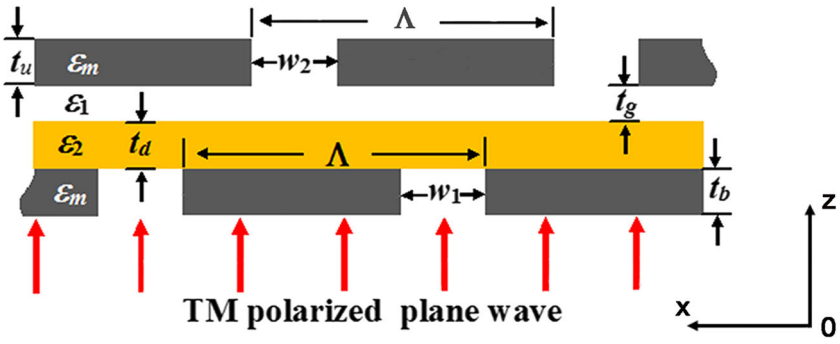


**Fig. 1** Basic geometry of the investigated plasmonic multilayer structure consisting of two longitudinally cascaded metallic nanogratings separated by an air separation (layer) $t_g$ and a dielectric layer of thickness $t_d$ and permittivity $\varepsilon_2$

inset of Fig. 2. Obviously, the transmission spectra present three resonant peaks as the slit of the upper nanograting is less than the width of $w_2 = 200$ nm, where two appear in the visible region and one in near-IR region. To be distinguishable, the three peaks are, respectively, marked as $P_1$, $P_2$, and $P_3$ in order of wavelength, from shortest to longest. In this case, the metal ridges of the upper nanograting are transversely butt-jointed with that of the bottom one to form MIM coupled waveguides. As $w_2$ decreases, the locations of the transmission peaks $P_1$ and $P_2$ are nearly unchanged and always remain at around 505 and 670 nm. Their optical transmittances can achieve 0.97 and 0.94, respectively, which indicates that the cascaded plasmonic nanograting structure is nearly transparent for the incident light at the two transmission peak wavelengths. For the transmission peak $P_3$, the shift of its wavelength displays a nonlinear dependence on $w_2$. Meanwhile, its transmission efficiency is enhanced with decreasing $w_2$ and can reach a maximum of 0.91. Notably, the transmission peak $P_1$ presents an ultra-narrow bandwidth of 20 nm, while the bandwidths of the other two transmission peaks $P_2$ and $P_3$ successively increase. With increasing $w_2$, the butt-jointed segment between the two cascaded nanogratings is diminished; the transmission peak $P_3$ becomes broader and lower and completely disappears at $w_2 = 250$ nm. When the upper nanograting slit enlarges to $w_2 = 350$ nm, the transmission peak $P_2$ also vanishes, leaving the peak $P_1$ alone in the transmission spectrum. At this moment, the butt-jointed segment between the two cascaded nanogratings reduces to zero. Continuing to enlarging $w_2$ beyond 350 nm, the metallic ridge of the upper nanograting becomes gradually less contribution to the transmission of light, while the bottom one with the high-permittivity dielectric layer plays a dominant role; hence, the transmission spectrum gradually becomes the same as the one in the inset of Fig. 2. In addition, there exist two transmission dips, donated as $D_1$ and $D_2$, and situated at between the three peaks. With increasing $w_2$, their wavelength positions and bandwidths are accommodated to the change of the three peaks. At the case of $w_2 = 150$ nm, the dips of $D_1$ and $D_2$, with the transmission efficiency of 0.02 and 0.15, are localized at 560 and 850 nm, respectively.

Compared with the case of the isolated bottom nanograting with the high-permittivity dielectric layer, the achieved three near-perfect transmission peaks for the cascaded plasmonic nanograting structure are emerging transmission phenomena,

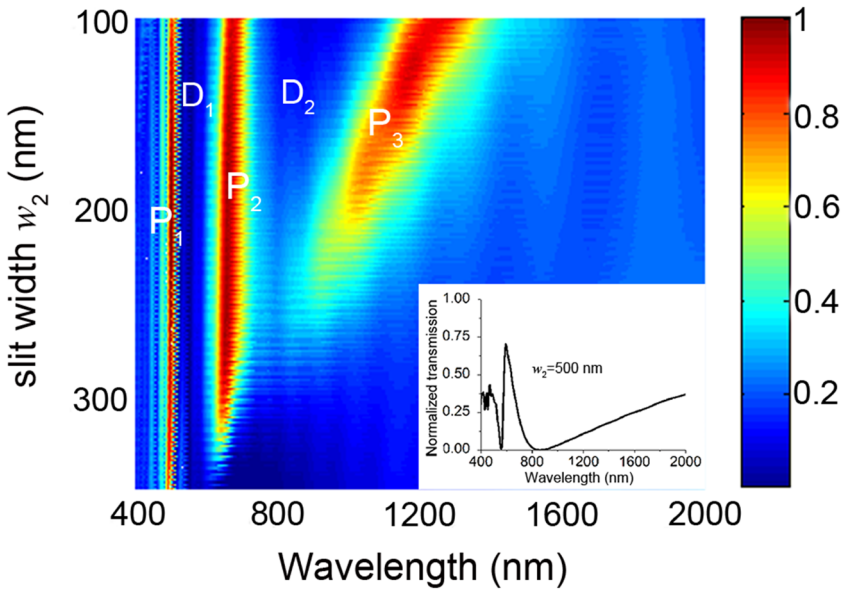


**Fig. 2** Calculated normalized transmissions of the cascaded plasmonic nanograting structure with respect to the wavelength and the slit width $w_2$ of the bottom nanograting in the case of fixed $w_1 = 150$ nm, $t_u = t_b = 30$ nm, $t_d = 50$ nm, $t_g = 25$ nm, $\Lambda = 500$ nm, and $\varepsilon_2 = 3.9$. $P_1$, $P_2$, and $P_3$ mark the transmission peaks; $D_1$ and $D_2$ denote the transmission dips. Inset gives the spectral transmission of the isolated bottom nanograting with the high-permittivity dielectric layer

which indicates that new plasmonic coupling mechanisms tend to occur between the two cascaded plasmonic nanogratings. The response of three transmission peaks to the variation of the slit width $w_2$ demonstrates that the essential underlying physics for them are distinguishable. Moreover, the near-perfect transmission behaviors of the cascaded plasmonic nanograting structure promise a perfect candidate for the plasmonic filter at visible and near-infrared frequencies.

To explore the physical mechanisms for the near-unity transmissions presented in Fig. 2, we take $w_2 = 150$ nm as an example to calculate the spatial distribution of EM field. Figure 3 displays the intensity plots of $|H_y|$ and $|E_x|$, as well as the corresponding phase plots of $\Phi(H)$ and $\Phi(E)$ within two periodic cells of the cascaded plasmonic nanograting structure for the transmission peak $P_1$ at the wavelength of $\lambda = 505$ nm. Obviously, on the transmission interfaces of the cascaded structure, the EM field distributions are in second-order standing-wave oscillating states, i.e., second-order resonance phenomena of SPP waves occur. As well, standing wave of SPP waves is formed on the incident interface of the cascaded structure as a consequence of the interference between the scatter fields with the incident light field. More importantly, the intensity of $H_y$ field is more prominently concentrated at the center of the slits than at the center of the ridges, which seems to be the physical reason for the near-unity transmissivity. Inside the MIM coupled waveguides, the $H_y$ fields localized on the top and bottom walls are also in the resonance state with the lower intensity, but they are not discontinuous and do not couple into a MIM waveguide mode. Inversely, they are, respectively, continuous with $H_y$ fields centralized at the output and input slit portions of the cascaded structure, which also can be inferred from the phase plot of Fig. 3c. Meanwhile, the phase plot demonstrates that the phase of $H_y$ fields at the two dislocated slit portions are completely opposite, which means that $H_y$ fields confined within the two cascaded nanogratings have anti-symmetric distributions. Therefore, a new hybrid anti-symmetric SPP leaky mode can be generated in the cascaded structure, and it should be responsible for the transmission peak $P_1$, being contrary to the transmission dips reported in the previous studies [8, 9]. In Fig. 3b, $E_x$ field is found to mainly localize on the output and input surfaces of the cascaded structure and support the occurrence of the SPP resonance. In this case, surface charges are not only accumulated at the corners but also evenly distributed across the input and output interfaces. These surface charges dynamically oscillate like dipoles and are dedicated to boosting the transmission efficiency. The phase variations of $E_x$ field across the two cascaded nanogratings provide evidences of the new hybrid anti-symmetric SPP leaky mode. The asymmetric distribution of EM field intensities on the two interface is physically originated from different dielectric environments for the two cascaded nanogratings.

For the transmission peak $P_2$ at $\lambda = 670$ nm, the calculated EM field distributions are displayed in Fig. 4. In contrast to the above observations, the $H_y$ field intensity is mainly concentrated within the MIM coupled waveguides. In each period, the $H_y$ field can form a second-order standing wave along the horizontal direction, where two anti-nodes are, respectively, confined at the top and bottom wall centers of the MIM coupled waveguides, while the nodes are situated at the butt-jointed segments. Therefore, this transmission peak wavelength is satisfied with the horizontal resonance conditions within one period. On the transmission and incident interfaces of the cascaded plasmonic nanograting structure, the $E_x$ fields are mainly localized around the corners of the nanograting ridge and they can induce surface dipoles along each surface of the rectangular ridge, which play a prominent role for the enhancement of the transmission peak $P_2$. While within the MIM coupled waveguides, surface charged induced by the $E_x$ fields are evenly distributed across the top and bottom walls, which act as a pump to transfer light from the incident side to the transmission one. In the plot of $\Phi(H_y)$ and $\Phi(E_x)$, the phases remain unchanged as longitudinally across the MIM coupled waveguides, suggesting an in-phase configuration for the two cascaded plasmonic nanogratings. The phase jump of $\pi$ within each period along the horizontal direction of MIM coupled waveguides provides an evidence for the second-order SPP resonance mode.

Figure 5 presents the calculated plots of EM field for the cascaded plasmonic nanograting structure at the transmission peak $P_3$ of $\lambda = 1130$ nm. In this case, the $H_y$ field is also observed to mostly concentrate within the MIM coupled waveguides. The fields are tightly confined on the top and bottom metallic walls and they joint together at the butt-jointed segments of the MIM coupled waveguides via the coupling of evanescent fields to generate a horizontal first-order resonance mode within one period, which can be evidenced by the corresponding phase plots. The $E_x$ field induces electric dipoles on each edge of the rectangular ridges, dedicating to boosting the transmission of light through the cascaded plasmonic nanograting structure.

In contrast, the intensity and phase plots of $|H_y|$ and $\Phi(H_y)$ within two periodic cells of the cascaded plasmonic nanograting structure at the two transmission dips of $\lambda = 560$ and 850 nm are displayed in Fig. 6. For the two transmission dips, it is similar that the $H_y$ field is observed to be mainly concentrated on the two interfaces of the bottom nanograting but is nearly blank on the upper one except for the unequal intensity and the different order SPP resonance mode on the top interface of the bottom nanograting. Meanwhile, it is inferred from the phase plots that the $H_y$ fields on the two interfaces of the bottom nanograting are completely in opposite phase, indicating anti-symmetrically distributed. Therefore, a hybrid anti-symmetric bound SPP mode is formed on the bottom nanograting, which is a short-range mode that suppresses

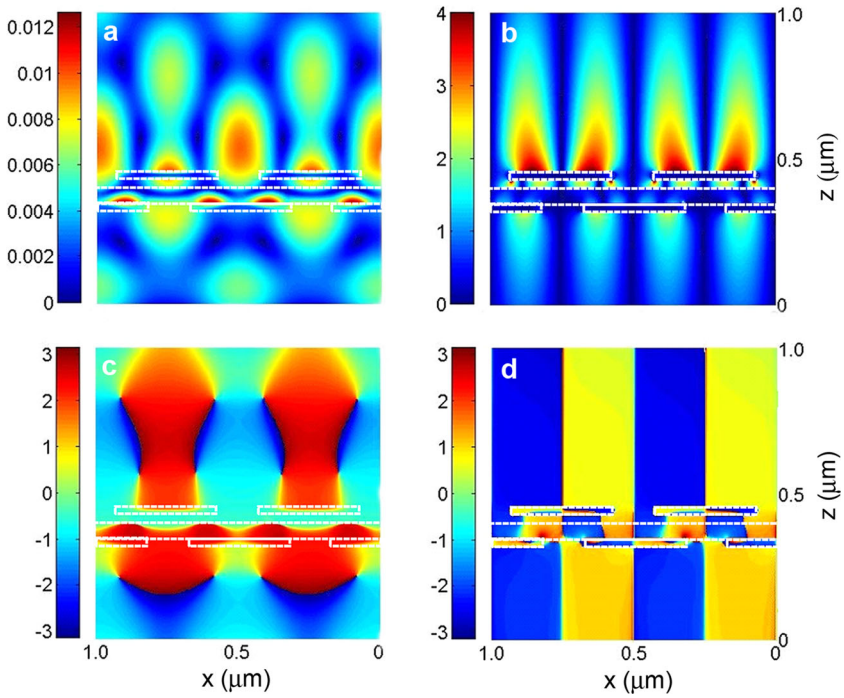


**Fig. 3** Calculated intensity (top panels) and phase (bottom panels) plots of magnetic field (left panels) and electric field (right panels) distributions within two periods of the cascaded plasmonic nanograting structure for the transmission peak $P_1$ at $\lambda =$ 505 nm. The parameters are fixed as $w_1 = w_2 = 150$ nm, $t_u = t_b =$ 30 nm, $t_d = 50$ nm, $t_g = 25$ nm, $\Lambda = 500$ nm, and $\varepsilon_2 = 3.9$. Panels **a**–**d** indicate $|H_y|$, $|E_x|$, $\Phi(H_y)$, and $\Phi(E_x)$, respectively. Among them the white dashed lines mark the zones of different materials

the light transmission through the upper grating, resulting in the dip in the transmission spectrum of Fig. 2 [27, 28].

Given the above EM field distributions, we propose the following explanations to explicitly understand the microcosmic transmission processes for the cascaded plasmonic nanograting structure. Upon irradiation of the plane wave light onto an individual ultrathin metallic nanograting deposited on a high-permittivity dielectric layer, SPP waves with different wave vectors are, respectively, excited on the metal/dielectric and metal/air interfaces, then they hybridize into an anti-symmetric SPP bound mode due to the fields overlapping within the ultrathin metal material. Under the resonance conditions, a standing wave for the anti-symmetric SPP bound mode is established, resulting in a nearly null optical transmission, as shown by the inset in Fig. 2. When another ultrathin metallic nanograting is

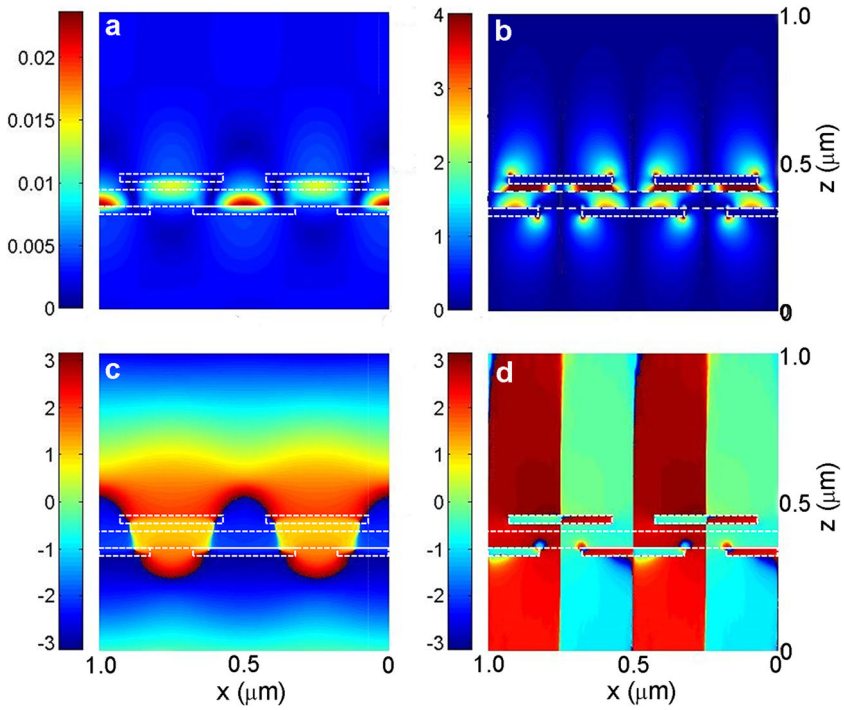


**Fig. 4** Calculated intensity (top panels) and phase (bottom panels) plots of magnetic field (left panels) and electric field (right panels) distributions within two periods of the cascaded plasmonic nanograting structure for the transmission peak $P_2$ at $\lambda =$ 670 nm. The parameters are fixed as $w_1 = w_2 = 150$ nm, $t_u = t_b =$ 30 nm, $t_d = 50$ nm, $t_g = 25$ nm, $\Lambda = 500$ nm, and $\varepsilon_2 = 3.9$. Panels **a**–**d** indicate $|H_y|$, $|E_x|$, $\Phi(H_y)$, and $\Phi(E_x)$, respectively. Among them the white dashed lines mark the zones of different materials

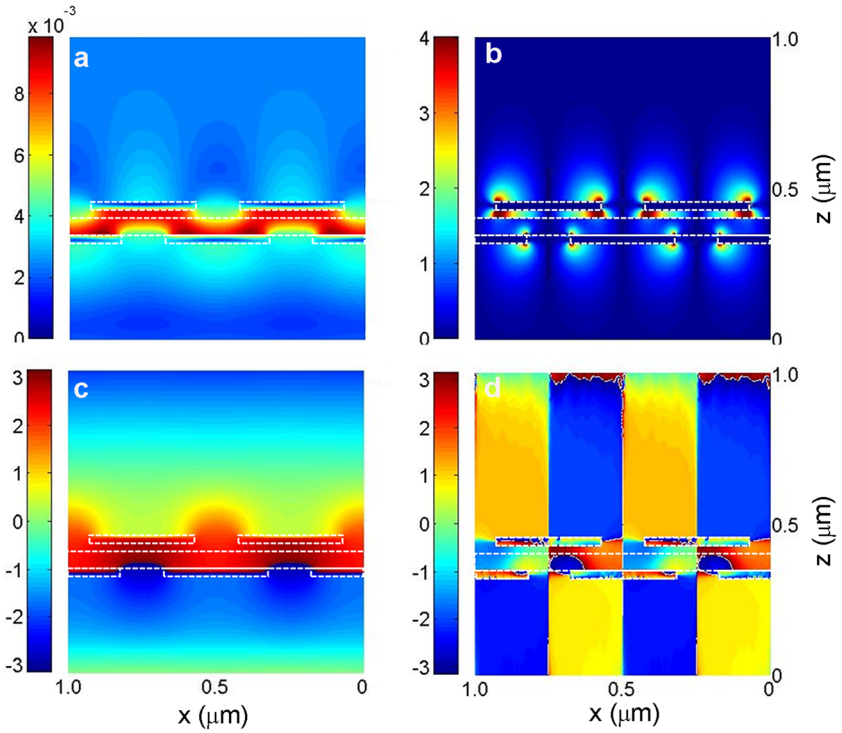


**Fig. 5** Calculated intensity (top panels) and phase (bottom panels) plots of magnetic field (left panels) and electric field (right panels) distributions within two periods of the cascaded plasmonic nanograting structure for the transmission peak $P_3$ at $\lambda =$ 1130 nm. The parameters are fixed as $w_1 = w_2 = 150$ nm, $t_u =$ $t_b = 30$ nm, $t_d = 50$ nm, $t_g =$ 25 nm, $\Lambda = 500$ nm, and $\varepsilon_2 = 3.9$. Panels **a**–**d** indicate $|H_y|$, $|E_x|$, $\Phi(H_y)$, and $\Phi(E_x)$, respectively. Among them the white dashed lines mark the zones of different materials

longitudinally cascaded with an air separation from the dielectric layer side to constitute two cascaded nanograting structure with their slits laterally dislocated a half-period, a series of horizontally butt-jointed MIM coupled waveguides are created between them. The SPP field localized on the metal/dielectric interface of the bottom nanograting acts as a secondary source to induce surface currents/charge on the upper nanograting, which can travel the light to the transmission side. On one hand, on the upper nanograting, the SPP mode with appropriate distribution of surface charges/currents is excited according to the geometrical shape. On the other hand, the SPP field excited on the upper nanogratings inevitably overlaps with that on the bottom nanograting, and this can modulates their original SPP modes into the new hybrid SPP modes based on the structural characteristics of the MIM coupled waveguides,

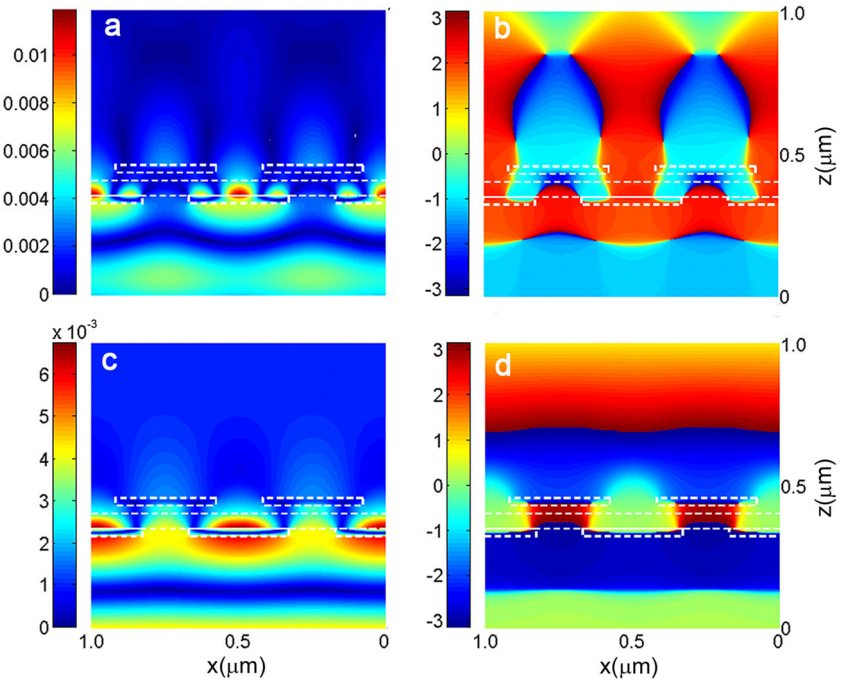


**Fig. 6** Calculated intensity (left panels) and phase (right panels) plots of magnetic field distributions within two periods of the cascaded plasmonic nanograting structure at the transmission dips of $\lambda = 560$ nm (top panels) and $\lambda = 850$ nm (bottom panels). Panels **a** and **c** indicate $|H_y|$; panels **b** and **d** represent $\Phi(H_y)$. The parameters are fixed as $w_1 = 150$ nm, $t_u = t_b =$ 30 nm, $t_d = 50$ nm, $t_g = 25$ nm, $\Lambda = 500$ nm and $\varepsilon_2 = 3.9$. Among them the white dashed lines mark the zones of different materials

which dedicates to the enhancement of light transmission through the cascaded plasmonic nanograting structure.

For the transmission peak $P_1$, the normal incident wave can excite two heterogeneous SPP bound waves on the bottom and upper nanogratings in sequence due to their asymmetric surrounding dielectric environment, as shown in Fig. 7a–d, and they can subsequently couple into a new hybrid anti-symmetric SPP leaky mode via the MIM coupled waveguides, resulting in the near-unity transmission efficiency. By the excitation of this hybrid anti-symmetric SPP leaky mode, the incident plane wave can maximumly couple into SPP wave on the incidence interface through satisfying the conservation of momentum, while SPP waves on the transmission interface match the resonance conditions to form a standing wave and simultaneously decouple into a radiating plane wave of the same frequency (or momentum) as the incident one, resulting in the near-unity transmissivity. Therefore, the wavelength of the transmission peak $P_1$ is quantitatively described by:

$$\lambda_0 = n_{\text{eff}} * \lambda_{\text{sp}} = n_{\text{eff}} * \Lambda \tag{1}$$

where $n_{\text{eff}} = \sqrt{\frac{\varepsilon_m \varepsilon_d}{\varepsilon_m + \varepsilon_d}}$ is the effective index of SPP wave on the incident and transmission interfaces. It can be easily inferred that the wavelength position of transmission peak corresponding to the hybrid anti-symmetric SPP leaky mode is mainly determined by the periodicity of the system and is nearly independent of the nanograting slit (or ridge) width, which coincides with the FDTD simulation results in Fig. 2. The efficiency of the transmission peak $P_1$ associated with this hybrid anti-symmetric SPP leaky mode is very sensitive to the two sandwiched heterogenous dielectric layers and the structural parameters, because once energies of the SPP waves localized on the upper and bottom nanogratings are not consistent, the coupling between them becomes less effective, leading to a reduction for the transmissivity of the hybrid anti-symmetric SPP leaky mode, which will be demonstrated in the next section.

In contrast to the case of the hybrid anti-symmetric SPP leaky mode, the transmission peak $P_2$ is associated with localized SPP waveguide resonance mode. At this case, the SPP waves excited on the upper and bottom nanogratings, as

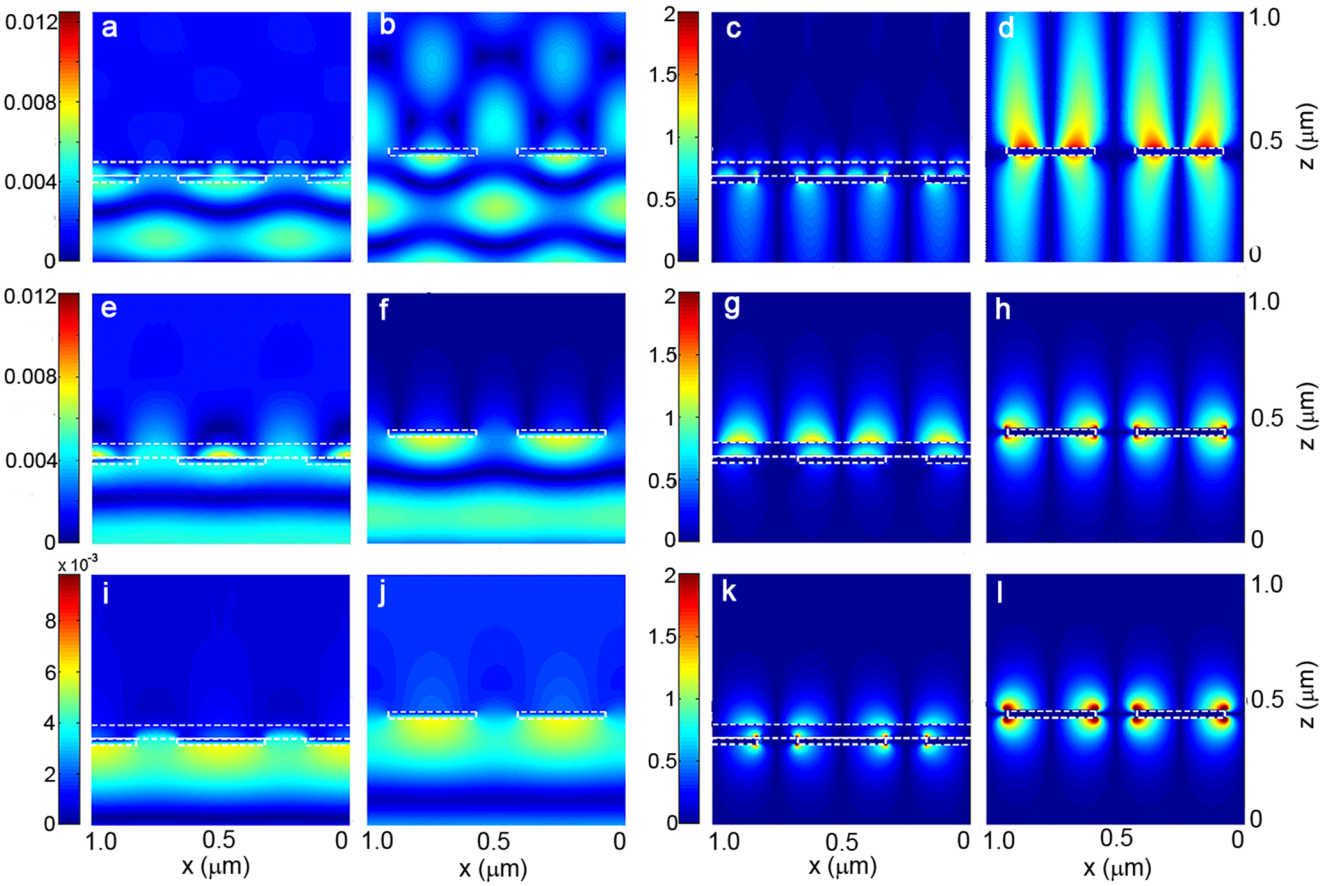


**Fig. 7** Calculated intensity plots of magnetic field (two left panels) and electric field (two right panels) distributions within two periods of the two isolated nanogratings at the three transmission peaks of $\lambda = 505$ nm (top panels), $\lambda = 670$ nm (middle panels), and $\lambda = 1130$ nm (bottom panels). Panels **a**, **b**, **e**, **f**, **i**, and **j** indicate $|H_y|$; panels **c**, **d**, **g**, **h**, **k**, and **l** represent $|E_x|$. Among them the white dashed lines mark the zones of different materials

shown in Fig. 7e–h, hybridize into a second-order localized SPP resonance mode within one period of the MIM coupled waveguides via the evanescent field coupling of SPP waves, resulting in the near-unity transmittance of 0.94. Within one period of the MIM coupled waveguides, this localized SPP resonance mode along the horizontal direction satisfies the following equation:

$$k_{sp1} \times w_2 + k_{sp2} \times w_1 + k_{sp-co} \times (\Lambda - w_1 - w_2) + \Delta\varphi = 2\pi \quad (2)$$

wherein $k_{sp1}$, $k_{sp2}$, and $k_{sp\text{-}co}$ are, respectively, the wave vectors of SPP waves localized on the top and bottom walls at the gap segment of MIM coupled waveguides and within the butt-jointed segment; $\Delta\varphi$ represents an abrupt phase change with a small magnitude at the edges of the nanograting ridge and it can be neglected. Therefore, the wavelength of the transmission peak $P_2$ associated with the localized SPP waveguide resonance mode can be approximately expressed by:

$$\lambda_0 = n_{eff1} \times w_2 + n_{eff2} \times w_1 + n_{eff-co} \times (\Lambda - w_1 - w_2). \quad (3)$$

Here, $n_{eff1} = k_{sp1}/k_0$, $n_{eff2} = k_{sp2}/k_0$, and $n_{eff-co} = k_{sp-cp}/k_0$ are, respectively, the corresponding effective index of SPP waves confined on each segment of the MIM coupled waveguides, which are strongly dependent on two sandwiched heterogenous dielectric layers. Importantly, since the nodes of the second-order SPP resonance mode are just situated at the butt-jointed segments, that is, SPP waves confined on the top and bottom nanogratings are discontinuous, the structural change of the butt-jointed segment has no significant influence on $n_{eff-co}$ as well as the wavelength position of the transmission peak $P_2$, which is in accordance with the $w_2$ independence of the wavelength position in Fig. 2. Hence, the wavelength position of the transmission peak $P_2$ associated with the second-order localized SPP waveguide resonance mode is highly sensitive to the high-permittivity dielectric layer and the system period.

Analogous to the case of the transmission peak $P_2$, under the incidence of plane wave at the wavelength of the transmission peak $P_3$, a horizontal first-order SPP resonance mode occurs within one period of the MIM coupled waveguides based on the hybridization between the SPP waves excited on the upper and bottom nanogratings, as shown in Fig. 7i–l. At this case, the effective optical path of the SPP waves within one period involves two components: one introduced by SPP wave propagating along the upper and bottom walls at the gap segment of the MIM coupled waveguides; the other introduced by SPP wave travel between the upper and bottom walls at the butt-jointed segment. Therefore, the SPP wave satisfies the following equation:

$$k_{sp1} \times w_2 + k_{sp2} \times w_1 + 2k_{sp-co} \times \Delta = \pi. \quad (4)$$

The wavelength of the transmission peak $P_3$ is quantitatively described as:

$$\lambda_0 = 2(n_{eff1} \times w_1 + n_{eff2} \times w_2 + n_{eff-co} \times 2\Delta) \quad (5)$$

wherein, $\Delta = \sqrt{(\Lambda - w_1 - w_2)^2/4 + (t_g + t_d)^2}$ is a function of the butt-jointed segment length, the thicknesses of the two sandwiched dielectric layers $t_d$ and $t_g$. Here, it stresses that $n_{eff-co}$ is dependent on $t_g$ and $t_d$ due to the coupling of SPP waves confined on the upper and bottom walls at the butt-jointed segment [29]. We can conclude that the transmission peak wavelength $P_3$ associated with the first-order localized SPP waveguide resonance mode is extremely sensitive to the two sandwiched dielectric layers and the system period.

In addition, the influences of both the structural parameters and the dielectric layer on the normalized spectral transmittance of the cascaded structure at normal incidence are also further investigated. Figure 8a shows the dependence of the normalized spectral transmittance on the system period of $\Lambda$. The other parameters are set as: $w_1 = w_2 = 150$ nm, $t_b = t_u = 30$ nm, $t_d = 50$ nm, $t_g = 25$ nm, and $\varepsilon_2 = 3.9$. It can be easily seen that the wavelengths of three transmission peaks are linearly red shifted with increasing $\Lambda$. When the transmission peak is associated with either the hybrid anti-symmetric SPP leaky mode or the localized SPP waveguide resonance mode, its wavelength position is always proportional to $\Lambda$, which is evidenced by the white curves in Fig. 8a obtained from Eqs. (1)–(5). Therefore, the wavelength positions of the three peaks can be easily controlled by mean of adjusting $\Lambda$. Note that the transmittance of the peak $P_1$ shows a non-monotonous variations with the increase of $\Lambda$ and achieves near-unity at around $\Lambda = 500$ nm. The reduction of the transmissivity with the period variation can be attributed to the non-degenerate of energies of the two SPPs mode localized on the upper and bottom grating, which can be reversed by appropriately modulating the dielectric permittivity $\varepsilon_2$. Besides, the bandwidths of the three peaks keep invariable with increasing $\Lambda$.

The normalized spectral transmittance for the cascaded plasmonic nanograting structure as a function of the air separation (layer) $t_g$ is displayed in Fig. 8b, where the other parameters are set as: $w_1 = w_2 = 150$ nm, $t_b = t_u = 30$ nm, $t_d = 50$ nm, $\Lambda = 500$ nm, and $\varepsilon_2 = 3.9$. For the transmission peaks $P_1$ and $P_2$ in the visible region, the wavelength positions are nearly non-sensitive to $t_g$, as predicted by the white dash and dash dot lines obtained from Eqs. (1) and (3). But their transmittances drop rapidly with increasing $t_g$, since the coupling efficiency of SPP waves from the bottom nanograting to the upper one dramatically declines. Finally, both the hybrid anti-symmetric SPP leaky mode and the second-order localized SPP waveguide resonance mode are hard to form when the two cascaded nanogratings are separated far enough, leading to the reduce of the transmittances of the corresponding peaks into null. As for the

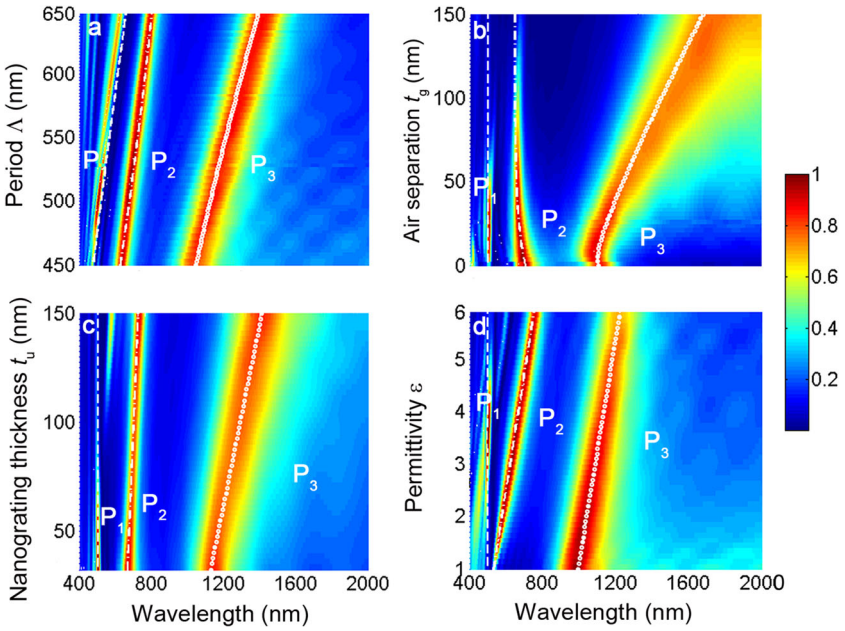


**Fig. 8** Calculated transmittance of the cascaded plasmonic nanograting structure as a function of the wavelength and **a** the system period Λ, **b** the air separation (layer) $t_g$, **c** the upper nanograting thickness $t_u$, and **d** the dielectric permittivity $\varepsilon_2$. The white dash, dash dot, and circle dot curves are, respectively, obtained from Eqs. (1), (3), and (5)

transmission peak $P_3$ in the near-IR region, the SPP wave confined on the bottom nanograting with a larger decayed length can still couple with that on the upper nanograting to induce the first-order localized SPP waveguide mode, which travels the incident light despite $t_g$ arrives at 150 nm. The increase of $t_g$ enlarges the optical path between the two cascaded nanogratings, leading to the red-shifted of the peak $P_3$ wavelength position, which is accord with the white circle dot curve obtained from Eq.(5), in accompany with its bandwidth broadening. Furthermore, the transmission peak $P_3$ also would be gradually fade away with continuously increasing $t_g$. On the other hand, decreasing $t_g$ to 0, the air layer disappears, resulting in symmetric dielectric surrounding environment for the two cascaded nanogratings. At this case, the peak $P_1$ drops rapidly to a low transmittance of 0.35, which is originated from the dispersion of the energies of two SPP modes on the upper and bottom nanogratings. For the peak $P_2$ and $P_3$, the symmetric dielectric environment has no influence on the formation of the associated localized SPP waveguide modes; they still be present in the transmission spectrum with near-unity transmittance.

The response of the spectral transmittance to variation of the upper nanograting thickness $t_u$ is demonstrated in Fig. 8c, where the other parameters are set as: $w_1 = w_2 = 150$ nm, $t_b = 30$ nm, $t_d = 50$ nm, $t_g = 25$ nm, $\Lambda = 500$ nm, and $\varepsilon_2 = 3.9$. Obviously, the increase of $t_u$ has no influence on the wavelength position of the peak $P_1$, as expected by the white dash line obtained from Eq. (1), but dramatically diminishes its transmittance. The reason is also ascribed to the non-degeneration of the energies of SPP modes confined on the upper and bottom nanogratings, which is originated from the decrease of the effective refraction index of the SPP mode confined on upper nanograting with the increase of $t_u$ [8, 30]. On the other hand, as for the transmission peaks $P_2$ and $P_3$ associated with the localized SPP MIM waveguide resonance modes, the increase of $t_u$ enlarges either the effective refraction index or the optical path of the localized SPP waveguide mode, resulting in red-shift of the wavelength position, which is consistent with the white dash dot and circle dot curves obtained from Eqs. (3) and (5).

Figure 8d presents the spectral transmittance for the cascaded plasmonic nanograting structure with variable permittivity $\varepsilon_2$ of the dielectric layer. The structural parameters are fixed as: $w_1 = w_2 = 150$ nm, $t_u = t_b = 30$ nm, $t_d = 50$ nm, $t_g = 25$ nm, and $\Lambda = 500$. It can be seen that transmittance of the peak $P_1$ associated with the hybrid anti-symmetric SPP leaky mode arrives at near-unity at around $\varepsilon_2 = 3.9$. As $\varepsilon_2$ increases or decreases, the peak $P_1$ remains at the wavelength position of $\lambda = 500$ nm, as predicted by the white dash line obtained from Eq. (1), but its transmittance drop rapidly accompanied with peak splitting phenomenon, which can be also attributed to the dispersion of the energies of two SPP modes on the upper and bottom nanograting. The point to emphasize here is that the transmission peak $P_1$ tends to shrink or disappear when $\varepsilon_2$ reduces to 1 (as well as the case of $t_g = 0$), that is, as two heterogeneous dielectric layers sandwiched between the two cascaded nanogratings degenerate into a homogeneous layer, the near-unity transmission peak $P_1$ is difficult to be formed. Hence, the two sandwiched heterogeneous dielectric layers between two plasmonic nanogratings is an essential factor for the appearance of the near-unity transmission peak $P_1$. Moreover, the increase of $\varepsilon_2$ introduce the reduction of the effective wavelength for SPP mode inside the MIM coupled waveguides and the growth of the optical

path between the two cascaded nanogratings, leading to the shift of the wavelength position of the transmission peaks $P_2$ and $P_3$ with respect to the localized SPP waveguide resonance modes, which coincides with the white dash dot and circle dot curves obtained from Eqs. (3) and (5).

## Conclusions

To summarize, we have comprehensively studied the optical transmission behaviors for two longitudinally cascaded ultra-thin metallic nanogratings with a lateral half-period dislocation and sandwiched with an air layer and a high-permittivity dielectric layer. Based on a series of horizontally butt-jointed MIM coupled waveguides formed between them, SPP waves excited on the two cascaded nanogratings can hybridize into two type modes via the coupling of evanescent fields: one is a new hybrid anti-symmetric SPP leaky mode undergoing surface interface resonance; the other is localized SPP mode undergoing waveguide resonance. Both of them make contributions to near-unity spectral transmission peaks but with different bandwidths. The appearance of the ultra-narrow bandwidth transmission peak associated with hybrid anti-symmetric SPP leaky mode essentially relies on the two heterogeneous dielectric environment inserted between the two cascaded nanogratings. The spectral transmission properties of the cascaded plasmonic nanograting structure perform a high degree of tunability by varying the structural parameters and the dielectric layer, which have significant implications on nano-optics devices, such as optical filtering, optical sensors, and nanoscale distance ruler.

**Funding Information** We acknowledge financial supports from the National Science Foundation of China (grant no. 11674178).

## References

1. Ebbesen TW, Lezec HJ, Ghaemi HF, Thio T, Wolff PA (1998) Extraordinary optical transmission through sub-wavelength hole arrays. Nature 391:667–669
2. Porto JA, Garcı'a-Vidal FJ, Pendry JB (1999) Transmission resonances on metallic gratings with very narrow slits. Phys Rev Lett 83:2845–2848
3. Martin-Moreno L, Garcia-Vidal FJ, Lezec HJ, Pellerin KM, Thio T, Pendry JB, Ebbesen TW (2001) Theory of extraordinary optical transmission through subwavelength hole arrays. Phys Rev Lett 86:1114–1117
4. Li XF, Yu SF (2010) Extremely high sensitive plasmonic refractive index sensors based on metallic grating. Plasmonics 5(4):389–394
5. Hao J, Wang J, Liu X, Padilla WJ, Zhou L, Qiu M (2010) High performance optical absorber based on a plasmonic metamaterial. Appl Phys Lett 96(25):251104
6. Yang XF, Zhang SX, Zhang DH, Wang YK, Wang J (2013) Subwavelength interference lithography based on a unidirectional surface plasmon coupler. Opt Eng 52(8):086109
7. Vincenti MA, Grande M, De Ceglia D, Stomeo T, Petruzzelli V, De Vittorio M, Scalora M, D' Orazio A (2012) Color control through plasmonic metal gratings. Appl Phys Lett 100(20):201107
8. Sun Z, Zuo X, Lin Q (2010) Plasmon-induced nearly null transmission of light through gratings in very thin metal films. Plasmonics 5: 13–19
9. Xiao S, Zhang J, Peng L, Jeppesen C, Malureanu R, Kristensen A, Mortensen NA (2010) Nearly zero transmission through periodically modulated ultrathin metal films. Appl Phys Lett 97: 071116
10. Liu T, Shen Y, Shin W, Zhu Q, Fan S, Jin C (2014) Dislocated double-layer metal gratings: an efficient unidirectional coupler. Nano Lett 14(7):3848–3854
11. Ma R, Liu Y, Yu Z, Zhang Y, Chen L, Wu D, Li Y, Ye H (2016) The sensing characteristics of periodic staggered surface plasmon gratings. Opt Commun 381:391–395
12. Jia Z, Shuai Y, Chen X, Tan H (2016) Double directions nanoscale range finding using Fano resonance in coupled gratings. Plasmonics 11:1331–1336
13. Wang C, Chang Y, Tsai D (2009) Spatial filtering by using cascading plasmonic gratings. Opt Express 17(8):6218–6223
14. Christ A, Zentgraf T, Tikhodeev SG, Gippius NA, Kuhl J, Giessen H (2006) Controlling the interaction between localized and delocalized surface plasmon modes: experiment and numerical calculations. Phys Rev B 74:155435
15. Wu J, Zhou C, Yu J, Cao H, Li S, Jia W (2014) Polarization-independent absorber based on a cascaded metal–dielectric grating structure. IEEE Photonics Tech L 26(9):949–952
16. Sun Z, Zuo X (2011) Tunable absorption of light via localized plasmon resonances on a metal surface with interspaced ultra-thin metal gratings. Plasmonics 6:83–89
17. Lei J, Ji B, Lin J (2017) High-performance tunable plasmonic absorber based on the metal-insulator-metal grating nanostructure. Plasmonics 12:1–6
18. Wang CM, Chang YC, Tsai MW, Ye YH, Chen CY, Jiang YW, Lee SC, Tsai DP (2008) Angular independent infrared filter assisted by localized surface plasmon polariton. Photon Technol Lett 20: 1103-1105
19. Wang CM, Chang YC, Tsai MW, Ye YH, Chen CY, Jiang YW, Lee SC, Tsai DP (2007) Reflection and emission properties of an infrared emitter. Opt Express 15:14673–14678
20. Wang W, Zhao D, Chen Y, Gong H, Chen X, Dai S, Yang Y, Li Q, Qiu M (2014) Grating-assisted enhanced optical transmission through a seamless gold film. Opt Express 22(5):5416–5421
21. Wang Z, Hou Y, Li W, Li X, Cai A (2016) Tunnel light through a continuous optically thick metal film utilizing higher order magnetic plasmon resonance. Plasmonics 11(6):1–6
22. Liu Z, Liu G, Huang K, Chen Y, Hu Y, Zhang X, Cai Z (2013) Enhanced optical transmission of a continuousmetal film with double metal cylinder arrays. IEEE Photon Technol Lett 25(12):1157–1160
23. Liu G, Hu Y, Liu Z, Chen Y, Cai Z, Zhang X, Huang K (2014) Robust multispectral transparency in continuous metal film structures via multiple near-field plasmon coupling by a finite-difference timedomain method. Phys Chem Chem Phys 16(9):4320–4328
24. Chen Y, Liu G, Huang K, Hu Y, Zhang X, Cai Z (2013) Enhanced transmission of a plasmonic ellipsoid array via combining with double continuous metal films. Opt Commun 311:100–106
25. Hu Y, G-q L, Z-q L, Y-h C, X-n Z, Z-j C, X-s L (2014) Robust double-spectral transparency of double mutually staggered plasmonic arrays sandwiched by two continuous metal films. Opt Commun 321:219–225
26. Ordal MA, Long LL, Bell RJ, Bell SE, Bell RR, Alexander RW, Ward CA (1983) Optical properties of the metals Al, Co, Cu, Au, Fe, Pb, Ni, Pd, Pt, Ag, Ti, and W in the infrared and far infrared. Appl Opt 22(7):1099–1119

27. Braum J, Gompf B, Kobiela G, Dressel M (2009) How holes can obscure the view: suppressed transmission through an ultrathinmetal film by a subwavelength hole array. Phys Rev Lett 103:203901
28. Yang FZ, Sambles JR, Bradberry GW (1991) Long-range surface modes supported by thin films. Phys. Rev. B 44:5855–5872
29. Collin S, Pardo F, Pelouard JL (2007) Waveguiding in nanoscale metallic apertures. Opt Express 15(7):4310–4320
30. Burke JJ, Stegeman GI, Tamir T (1986) Surface-polariton-like waves guide by thin lossy metal films. Phys Rev B 33:5186–5201